PUBLICATIONS OF THE ASTRONOMICAL SOCIETY OF THE PACIFIC, **116**:1061–1071, 2004 November

The Four-Quadrant Phase Mask Coronagraph. IV. First Light at the Very Large Telescope

A. BOCCALETTI

LESIA, Observatoire de Paris-Meudon, 5 Place Jules Janssen, F-92195, Meudon, France; anthony.boccaletti@obspm.fr

P. RIAUD

Institut d'Astrophysique et de Géophysique de Liège,17 Allée du 6 Août, Bat. B5c, B-4000 Liège, Belgium; riaud@astro.ulg.ac.be

P. BAUDOZ, J. BAUDRAND, D. ROUAN, D. GRATADOUR, AND F. LACOMBE

LESIA, Observatoire de Paris-Meudon, 5 Place Jules Janssen, F-92195, Meudon, France; pierre.baudoz@obspm.fr, jacques.baudrand@obspm.fr, daniel.rouan@obspm.fr, damien.gratadour@obspm.fr, francois.lacombe@obspm.fr

AND

A.-M. LAGRANGE

Laboratoire d'Astrophysique, Observatoire de Grenoble, BP 53, F-38041 Grenoble Cedex 9, France; anne-marie.lagrange@obs.ujf-grenoble.fr

Received 2004 July 16; accepted 2004 September 8; published 2004 October 25

ABSTRACT. We present the first high-contrast images obtained at the ESO Very Large Telescope using a four-quadrant phase mask coronagraph. The two-night commissioning was carried out in 2004 January on NACO, the near-IR camera with adaptive optics at UT4. We evaluated the behavior of the coronagraph on a variety of astrophysical targets: binary stars, circumstellar disks, and active galactic nuclei. The performance of the coronagraph is in agreement with our expectations based on numerical simulations. The phase mask provides a stellar peak attenuation of a factor of about 10 on average (for long exposure), and its performance is limited only by the phase residuals (mainly low-order aberrations) that are left uncorrected by the adaptive optics system.

1. INTRODUCTION

The recent indirect discovery of planetary objects orbiting around an ever-growing number of nearby stars has motivated the development of instrumental techniques to perform direct detection of the few photons emitted from exoplanets. The main scientific motivation is oriented toward the understanding of planetary formation and evolution. Direct detection is quite challenging, since planets are much fainter and angularly close to their host star, while current telescopes and instruments are still unable to achieve high contrast at such angular separation. Coronagraphy is one of the promising techniques that could efficiently contribute to planet detection. The generic principle is quite simple and is based on the solar coronagraph invented by B. Lyot (1939) to observe the solar corona. In the last decade, several techniques have been proposed (Gay & Rabbia 1996; Roddier & Roddier 1997; Nisenson & Papaliolios 2001; Kuchner & Traub 2002) to suppress the starlight more efficiently than with a simple Lyot coronagraph. Among those techniques, our group is developing a phase-mask coronagraph proposed by some of us (Rouan et al. 2000), called the four-quadrant phase-mask (FQPM). The focal plane is split into four equal areas, two of which are phase-shifted by π. As a consequence, a destructive interference occurs in the relayed pupil, and the on-axis starlight rejected outside the geometric pupil is filtered with an appropriate diaphragm called the Lyot stop. The advantage over the Lyot mask is twofold: (1) no large opaque area at the center, and (2) a larger achievable contrast if good optical quality is met. With a full circular aperture and no aberrations, the FQPM delivers perfect starlight suppression. However, in its simplest version, this coronagraph is chromatic, since the π phase shift is performed at a single wavelength.

Our group at the Observatoire de Meudon is participating in several projects related to the direct imaging of exoplanets. The capabilities of the FQPM have been studied from a theoretical point of view (Rouan et al. 2000; Riaud et al. 2001; Boccaletti et al. 2002) and in the lab (Riaud et al. 2003). With our optical breadboard we achieved peak attenuation on the central source of about 10^5 at visible wavelengths and a contrast of 10^6 at $3\lambda/D$. Currently, we are involved in the *James Webb Space Telescope*/Mid-IR Instrument (MIRI) European consortium and are responsible for the study, manufacture, characterization, and delivery of a set of coronagraphic devices for the mid-IR imager (Boccaletti et al. 2003). We are also participating in the Lagrange et al. consortium for the phase-A study of a planet finder for the VLT (Mouillet et al. 2003).

In this context and in agreement with ESO, we installed

an infrared FQPM inside the near-IR+AO camera NACO (Rousset et al. 2003) on UT4 at the VLT in 2003 August. We were allocated a two-night commissioning run on January 1 and 2 to further assess the performance of the FQPM and to calibrate the system, plus two nights in 2004 April to observe circumstellar disks around pre–main-sequence stars. The FQPM is optimized for the *K* band. Given the seeing conditions, achromaticity is not required here, since the nulling degradation introduced by the residual phase defects after adaptive optics (AO) compensation is about 30 times larger than the limitation set by the chromatism. For the same reason, the presence of a central obscuration in the telescope aperture is not critical.

The data collected during the commissioning phase are presented in this paper, which is organized as follows: § 2 gives the intrinsic characteristics of the coronagraph, § 3 evaluates the performance obtained with either a reference source or an actual star, and finally, § 4 presents the first results on astrophysical objects. Conclusions are drawn in § 5.

2. CHARACTERISTICS

2.1. Definition of Metrics

It is important to first define the metrics used to characterize the ability of a coronagraph to suppress the on-axis starlight. With the increasing number of publications related to coronagraphy, several parameters may be considered, depending on the authors. Here we decided to use the following definitions:

Total rejection: Ratio of total intensity of the direct image to that of the coronagraphic image. The total rejection only gives the global attenuation of the on-axis object but can be easily compared to analytic calculations.

Peak attenuation: Ratio of the maximum of the direct image (at $\rho = 0$) to that of the coronagraphic image.

Contrast: Ratio of the maximum of the direct image (at $\rho = 0$) to the intensity of the coronagraphic image at a given separation ρ, azimuthally averaged.

These metrics are not necessarily related, so it is important to consider all of them to accurately assess the performance of the coronagraph.

2.2. Operating Wavelength

The FQPM was manufactured by the Fresnel Institute. A layer of SiO_2 was deposited onto a SiO_2 substrate. The four-quadrant design was obtained with a photolithographic technique, achieving an accuracy of a few microns. The thickness (e) and optical index (n) of the deposited layer is calculated to provide a π phase shift at the operating wavelength λ_0 according to the relationship

$$\phi = 2\pi(n-1)e/\lambda_0. \quad (1)$$

This causes a degradation of the rejection rate as a function of the wavelength (Riaud et al. 2003):

$$\tau(\lambda) = \frac{4}{\pi^2}\left(\frac{\lambda}{\lambda - \lambda_0}\right)^2, \quad (2)$$

where τ is the ratio of the total intensity of the point-spread function (PSF) to that of the FQPM image. The mask wavelength λ_0 was first measured in our laboratory before being shipped to the VLT in Paranal, Chile. Our coronagraphic setup at the Observatoire de Meudon operates at visible wavelengths and at room temperature (300 K). A grating was installed immediately after the coronagraphic image in a pupil plane. This setup allows us to measure phase masks operating at any wavelength longer than ~0.5 μm, since the general phase shift condition is actually $\phi = (2k + 1)\pi$, where k is an integer. The measured wavelength is then extrapolated at cryogenic temperatures (77 K) as long as the dependency of the optical index of the material on temperature is well known from previous calculations (Matsuoka et al. 1991). We compared the spectrum of the artificial off-axis source with that of the source centered on the coronagraph. The ratio of these two spectra reveals the destructive interferences caused by the π phase shift (Fig. 1). Since we were using a linear disperser, the spectral calibration was simply obtained in two points with two separate lasers at 0.6328 and 0.5320 μm, respectively, feeding exactly the same optics as the white light source. This first measurement yielded a central wavelength of 0.748 μm $\pm$ 0.25 nm for $k = 1$ in the visible, which was extrapolated to 2.154 μm $\pm$ 5 nm at room temperature for $k = 0$, and then to 2.146 μm $\pm$ 5 nm at 77 K.

The mask was also measured at Paranal when installed inside NACO. The same procedure was carried out on an artificial source (a fiber) inside NAOS (Nasmyth Adaptive Optics System). Two spectra in and out of the mask were recorded with the NACO grism. In that case, the dispersion was no longer linear, and calibration was obtained on a spectral lamp providing Argon emission lines. The resulting spectra are shown on Figure 1. The spectra were fitted with a parabola (as expected from theory; eq. [2]), and we measured a central wavelength of 2.143 μm $\pm$ 10 nm, in good agreement with the measurement we did in the laboratory at visible wavelengths. The FQPM operating wavelength is therefore well centered in the *K*-band filter.

2.3. Focus

The 3 mm thickness of the FQPM substrate adds a defocus in the beam that has to be compensated for with the deformable mirror. The theoretical value of this defocus is $(n - 1)e$, which is about -1.3 mm, according to the optical index of SiO_2 ($n = 1.43412 \pm 3 \times 10^{-5}$ at 77 K). Measurements obtained for a natural star with good correction are in agreement with this value.

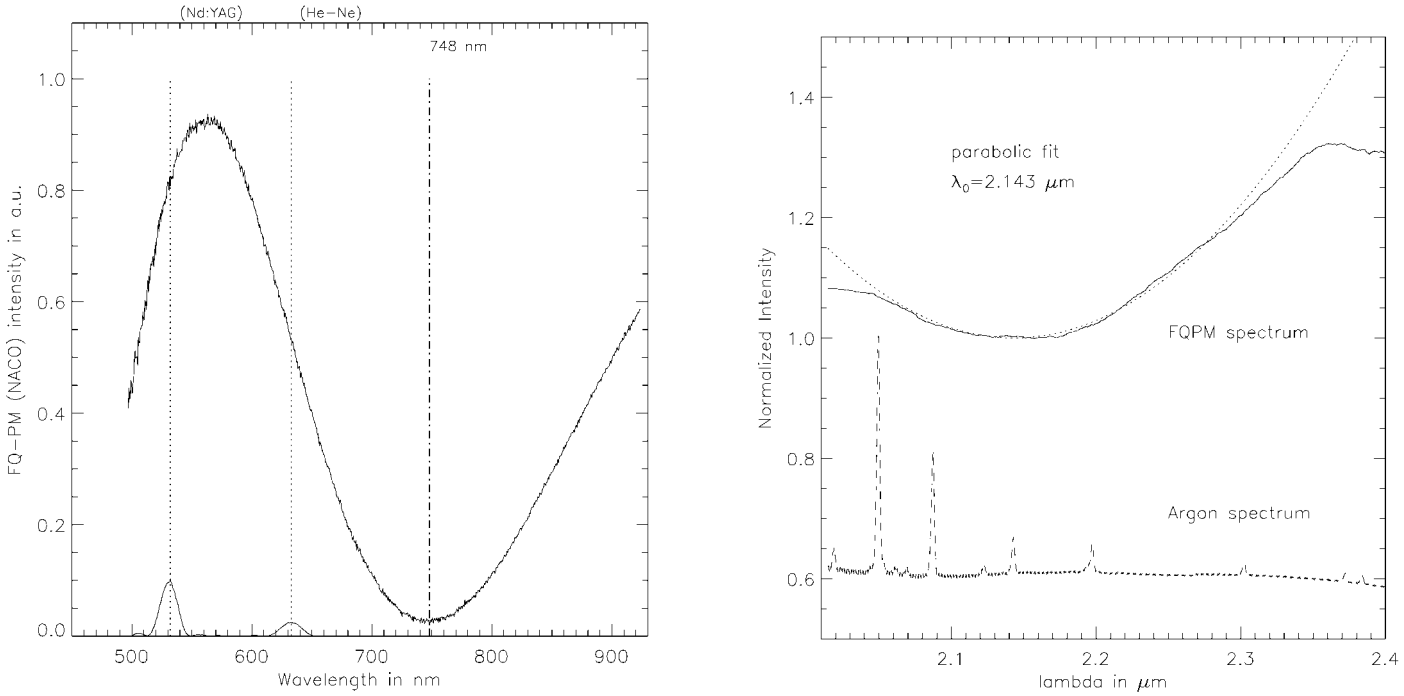

FIG. 1.—Spectra of the FQPM obtained in our laboratory at visible wavelengths (*left*) and inside NACO in the IR (*right*). The curves represent the residual light intensity vs. wavelength as measured in a setup in which light is dispersed with a grating. Once visible data are extrapolated to near-IR, the agreement of these two measurements is perfect (about 0.1%) and yields a central wavelength of 2.143 μm $\pm$ 10 nm. The spectral profile of π phase shifts was fitted with a parabola, as expected from eq. (2).

2.4. Radial Attenuation for Off-Axis Objects

The FQPM has no physical mask in the focal plane, unlike classical Lyot masks. However, the intensity of off-axis objects is reduced very close to the mask. The peak attenuation of an off-axis object is not as steep as with a hard-edged Lyot mask and mainly resides within the first λ/D. Nevertheless, it is critical to know how much flux is removed from an off-axis object like a companion to recover its actual photometry. The radial attenuation was measured on both a natural star and the artificial source. The source was shifted from the center and moved outward. The step was 1 pixel (13 mas) for the natural star and 0.1 pixel on the fiber in the first fraction of the Airy peak. In both cases the source was shifted on the *X*-detector axis, corresponding to an orientation of about 35° with respect to the edge of the closer quadrant. The data in Figure 2 show the peak attenuation of the source as a function of the angular separation with respect to the center of the mask. For the natural star, the data do not perfectly match the theoretical curves (especially within λ/D), which are calculated for a perfect wave front. However, for the fiber, the shape of the data curve matches perfectly with the theoretical curve. We confirmed with some binaries that theoretical curves yield an accurate calibration to within 10% for separations larger than λ/D.

2.5. Attenuation along the Mask Transition

The edges of the FQPM extend over the whole focal plane and can therefore reduce the intensity of an off-axis source if one falls right on this phase transition. These areas are not blind, but we measured a flux loss of about 1 mag (integrated over the Airy peak) for a source located on the transition. Two- and four-quadrant images are shown in Figure 3 for comparison.

2.6. Flat Field

Since the FQPM is deposited onto a substrate and installed at the focal plane, this optical element is expected to change the flat field. Flat fields were obtained with and without the mask in the K_s filter and with the 13 mas pixel^{-1} sampling. Figure 4 shows the flat field of the detector with the mask in the beam. These two flats were not recorded at the same time, so there could be differences caused by variations unrelated to the mask itself. Despite a cleaning before installation, the mask features many particles that create dark spots on the flat field. A brighter feature, possibly due to a reflection, is also present at the top of the image. Dark features are at maximum 20% below the detector flat field, and bright features at 10% above. The origin of the dark spots is not fully understood, although

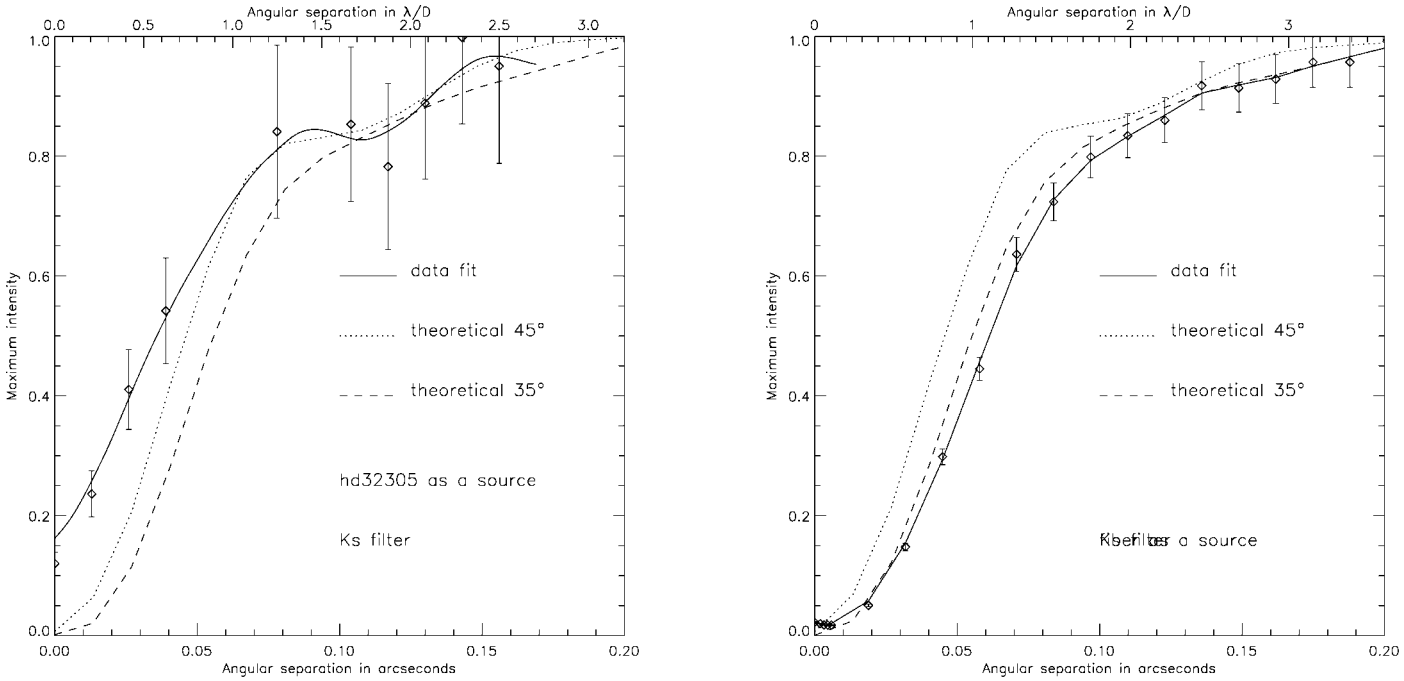

FIG. 2.—Radial attenuation of an off-axis object as measured on a natural star (*left*) and on the fiber (*right*), moved along a line 35° from one quadrant border. The solid line represents a smooth fit to the data; the dotted and dashed lines are theoretical attenuations at 45° and 35°, respectively. The error bars indicate the uncertainty of the data-curve normalization with respect to the theoretical curves. Data were obtained with a K_s filter and 13 mas pixel^{-1} sampling.

they could be dust particles that filtered into CONICA during implementation. Ideally, flat-field correction should include the features observed on the mask. However, in real conditions the focal plane is not stable on the detector; it moves because of flexures in the optics during observations. So the flat-field correction that includes FQPM features is efficient only on short observations (lasting a few minutes), but definitely not on long ones (~1 hr). However, a flat field with the FQPM in the beam is always needed to find the center of the mask and to perform target centering at the beginning of each target observation.

3. PERFORMANCE

3.1. Theoretical Performance

The most convenient parameter for comparing actual and theoretical performance is the total rejection of a coronagraph, since it can be written analytically. At the first order, total rejection is simply given by $4/d\phi^2$ (Riaud et al. 2003), where $d\phi$ is the amplitude of the phase aberrations. The total rejection corresponds to the ratio of the star intensity without the FQPM to that of the star with the coronagraph. In the data, we measured a total rejection ranging between 2 and 4 for a coherent energy ($E_c \approx e^{-d\phi^2}$) between 0.2 and 0.4. These values are in

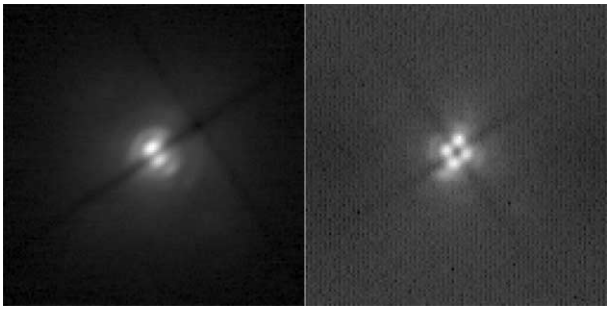

FIG. 3.—Two-quadrant (*left*) and four-quadrant (*right*) images of residuals for HD 32305 obtained in the K_s band. The intensity scale is not identical on both images. For comparison, the PSF peak attenuation is 3.9 on the two-quadrant image and 8.1 on the four-quadrant image.

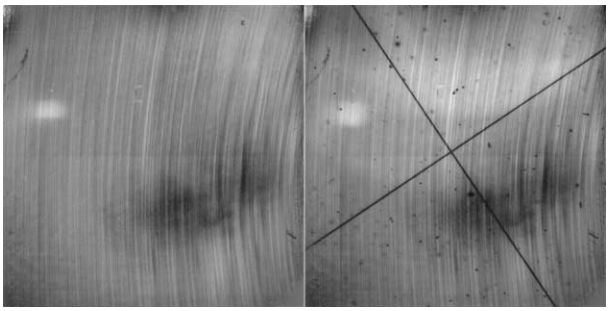

FIG. 4.—Flat field of the detector with the K_s filter and a sampling of 13 mas pixel^{-1} (*left*) and flat field obtained with the FQPM (*right*). Note the trace of the quadrant transition.

TABLE 1
THEORETICAL TOTAL REJECTION OF THE FQPM AS A FUNCTION OF THE COHERENT ENERGY

E_c	0.2	0.3	0.4	0.5	0.6	0.7	0.8
Rejection	2.5	3.3	4.4	5.8	7.8	11.2	17.9

agreement with theoretical values given in Table 1, although they are slightly lower. As indicated in § 2.1, the total rejection describes the flux attenuation over the whole focal plane and is not very dependent on the power spectrum density of phase aberrations. Among those aberrations, the tip-tilt is certainly the most limiting for a coronagraph like the FQPM. On NACO, the residual tip-tilt can be as large as 15–20 mas, which corresponds to about 0.27–0.36λ/D in the K band.

For the artificial source (fiber), we obtained a total rejection of about 16, which is again in agreement with $E_c \approx 0.8$ (the artificial source is diffraction limited). Theoretical calculations also demonstrate that the spectral bandwidth is not a limitation as long as the Strehl ratio is lower than ~0.8. Indeed, the narrowband filter NB2.17 and the broader K_s filter provide a theoretical total rejection of 43,000 and 175, respectively, much larger than what is measured on actual data (natural star or fiber source).

3.2. Comparison with Spectral Resolution

We analyzed the performance of the FQPM in different filters with several spectral resolutions, but based on the operating wavelength of the mask: SK ($\lambda/\Delta\lambda = 2.8$), K_s ($\lambda/\Delta\lambda = 6.2$), and NB2.17 ($\lambda/\Delta\lambda = 94.2$); and also in the H band ($\lambda = 1.66$ μm, $\lambda/\Delta\lambda = 5.0$), which is not optimized to the mask wavelength. This test was performed on the NAOS fiber; otherwise, the rejection rate would have been too small to show a variation of the attenuation factor. The peak attenuation is about 60–70 for filters NB2.17 and K_s, 25 with the SK, and only 7 in the H band. These numbers have to be compared with the attenuation measured for a natural star. In the current atmospheric conditions, we were not able to reach a central attenuation larger than about 10. Even the H-band filter would result in a modest attenuation of about 4 in real atmospheric conditions. Of course, as the Strehl ratio increases, the gain increases with narrowband filters centered on the operating wavelength. Finally, it is very important to note that the NB2.17 and K_s filters reach the same performance on the fiber, because even at such Strehl ratios (about 70%–80% on the fiber), the bandwidth effect is not as dramatic as the wave-front phase distortion. Therefore, we recommend observations be carried out in the K_s filter as long as the stellar flux allows (no saturation). The radial profiles are presented in Figure 5.

3.3. Comparison to Lyot Coronagraph

NACO includes diaphragms specifically designed to stop down the pupil, as required for a Lyot coronagraph. The simplest stop ("full undersized") is a hole with a diameter that is 90% that of the NACO pupil with the central obscuration unblocked. More sophisticated stops ("apodized") are similar but have an oversized central obscuration and trapezoidal spiders to allow pupil rotation during the observation. The star HD 6628 was observed with the IB2.18 filter ($\lambda = 2.18$ μm, $\lambda/\Delta\lambda = 36.3$) with both the FQPM and the Lyot mask (0.″7 in diameter), successively using the full undersized and the apodized stops. Images are presented in Figure 6. The FQPM images result in a combination of 40 exposures of 1 s, and the Lyot images were obtained by averaging four 10 s frames. The PSF was observed in similar conditions with 0.2 s exposures.

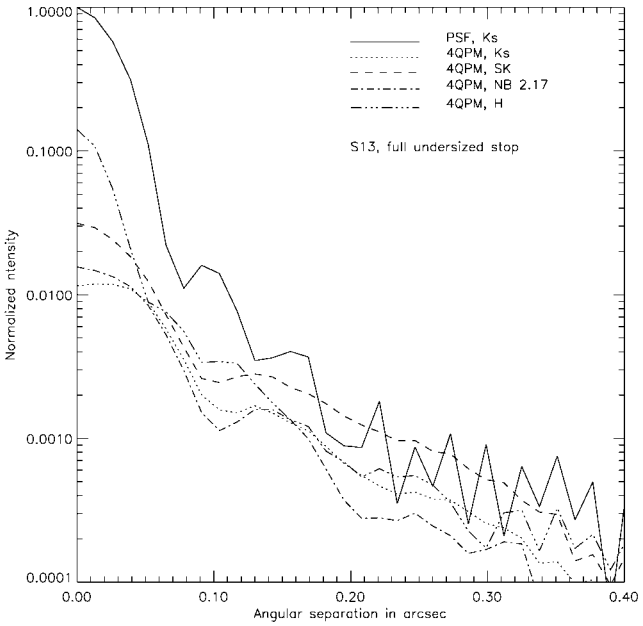

FIG. 5.—Radial profiles (azimuthally averaged) of PSF and coronagraphic images as measured in several filters: H, SK, K_s, and NB2.17.

The apodized stop correctly removes the diffraction spikes and reduces the rings around the FQPM. Radial profiles have been calculated and are presented in Figure 7. These plots show the advantage of the FQPM, which is able to get closer to the

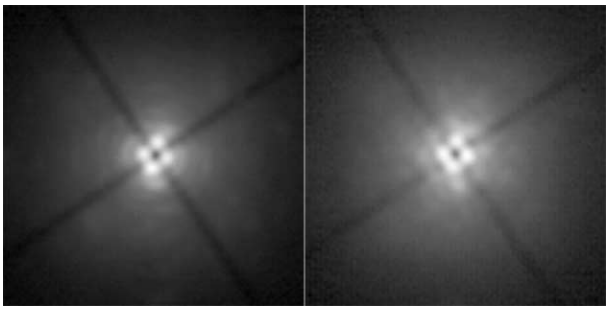

FIG. 6.—FQPM images with a full undersized stop (*left*) and an apodized stop (*right*). The field of view is 1.″5. Not a linear intensity scale ($I^{0.3}$).

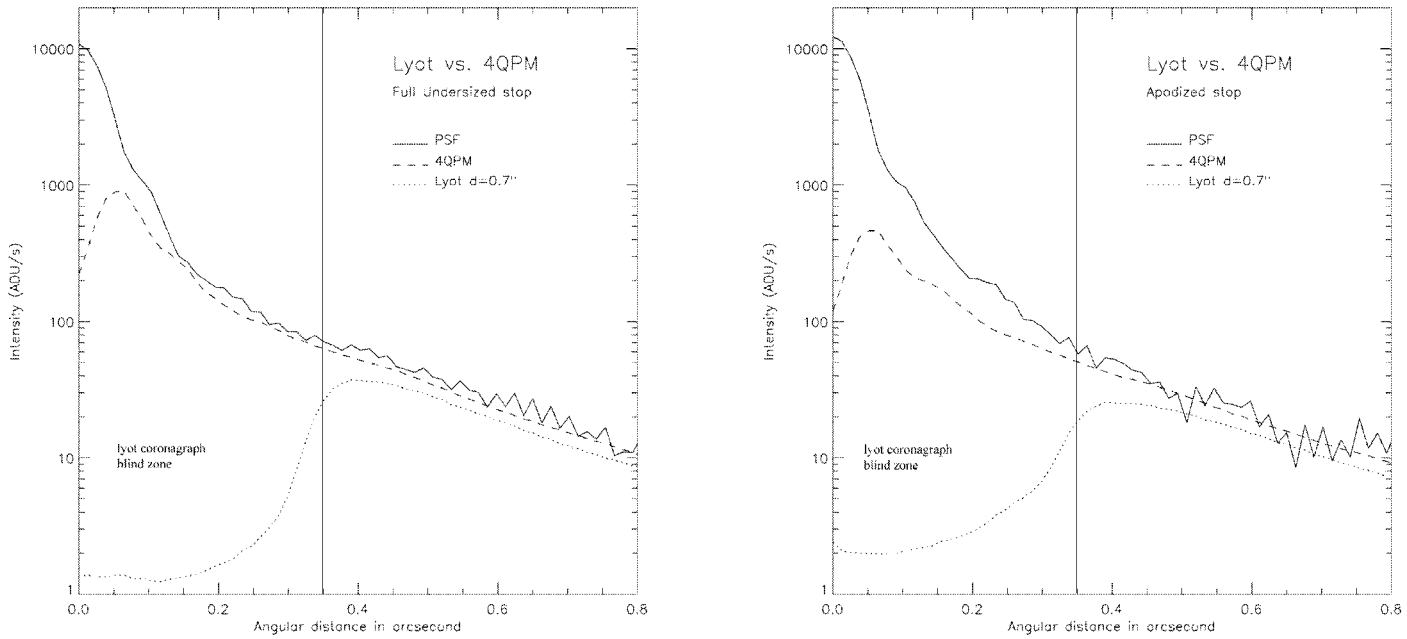

FIG. 7.—Radial profiles of the PSF (*solid line*), the FQPM image (*dashed line*), and the Lyot image (*dotted line*) with a full undersized (*left*) and an apodized stop (*right*). With the FQPM, the apodized stop allows a larger contrast than the PSF up to 0.″4, instead of 0.″2 with the full undersized stop. Vertical lines indicate the blind zone of the Lyot coronagraph, owing to the opaque mask.

star than the Lyot. The FQPM profile is formed by a diffraction residual at λ/D (caused by the residual tip-tilt), and then the halo is mostly parallel to the wings of the PSF, since it is dominated by speckle noise. The Lyot profile is always dominated by the speckled halo at any separation. However, at the angular radius achievable with the Lyot, both coronagraphs are equivalent in terms of contrast. Nevertheless, for large radii, the Lyot allows deeper integration, since more stellar flux is removed from the center, thus reducing the impact of the readout noise. The use of an apodized stop improves the central peak attenuation by a factor of about 2.2 and 1.7 on average, respectively, for the FQPM and the Lyot. Improvement is larger for the FQPM than for the Lyot, because the secondary mirror diffracts much more inside the pupil with a FQPM. Figure 8 shows the images of the two stops we used. The apodized stop has two positive effects: it reduces the background from the secondary mirror, and it blocks the diffraction around the pupil edges (secondary mirror, spiders) when a coronagraph is in use. In practice, the use of such a stop requires control of the alignment of the telescope pupil, especially close to zenith (pupil rotation is faster). However, the apodized stops do not match the pupil perfectly, because the NACO pupil is shifted by about 5.7% of its diameter with respect to that of the telescope. Recently, a baffle has been added to the secondary support of UT4, making the apodized stops less efficient, since the pupil matching is even less perfect.

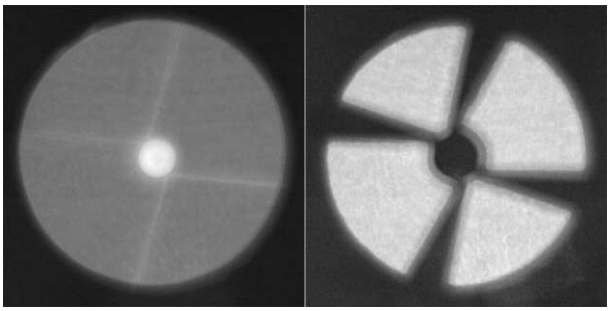

FIG. 8.—Images of the pupil through the full undersized stop (*left*) and the apodized stop (*right*). The telescope and NACO pupil are misaligned by 5.7% of the full diameter.

4. SCIENCE VERIFICATION

4.1. Binary Stars

Binary stars are among the most demonstrative objects for high-contrast coronagraphs like the FQPM. Targets were selected from the *Hipparcos* Catalogue (Perryman et al. 1997). Binary stars were chosen with an angular separation ranging between 0.″1 and 0.″4, which corresponds to the inaccessible area for the Lyot coronagraph. The brightness ratio between the primary and the secondary is lower than 3 mag in the visible. The brightness ratio in the near-infrared is unpredictable, since the spectral type of each component is unknown.

4.1.1. HIP 1306

HIP 1306 is classified as a binary star that turned out to be a triple object in our data, although we do not have evidence of a physical link with the third component. It was observed

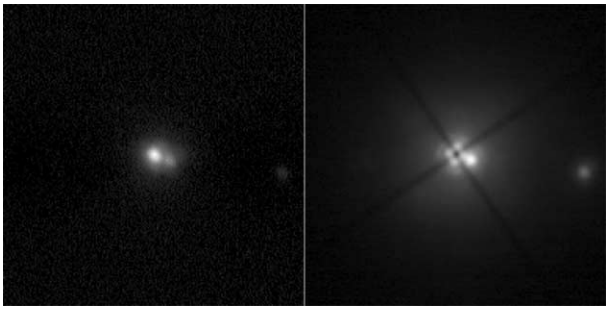

FIG. 9.—HIP 1306 PSF (*left*) and FQPM image (*right*). The exposure time is 60 s for the coronagraphic image and 4 s for the PSF. Not a linear intensity scale ($I^{0.5}$). FOV is 1.″25. North is up.

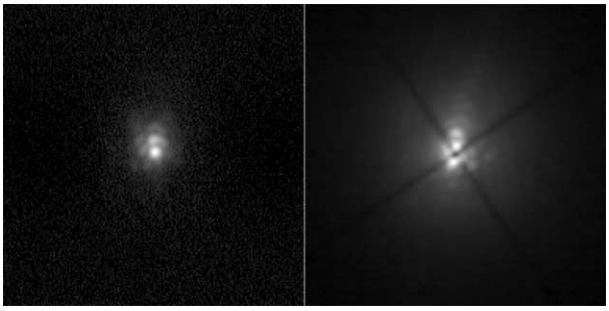

FIG. 10.—HIP 27758 PSF (*left*) and FQPM image (*right*). The exposure time is 80 s for the coronagraphic image. Not a linear intensity scale ($I^{0.5}$). FOV is 1.″25. North is up.

with the IB2.18 ($\lambda = 2.18$ μm, $\lambda/\Delta\lambda = 36$) filter with a full undersized stop. The Strehl ratio with AO compensation was about 28% (seeing 0.″9). The angular separations of components are 0.″128 and 1.″075 (Fig. 9). The closer companion photometry is strongly affected by the FQPM but can be recovered using the FQPM radial attenuation (Fig. 2). Brightness ratios measured on the FQPM image are respectively 1.6 and 3.5 mag, once corrected for FQPM attenuation. Although the companion is already detectable on direct imaging, the signal-to-noise ratio is definitely improved with the coronagraph at close radii, since the contrast is better, and at large radii because integration is deeper.

4.1.2. HIP 27758

The binary star HIP 27758 was observed with the IB2.12 ($\lambda = 2.12$ μm, $\lambda/\Delta\lambda = 35$) filter with a full undersized stop and a large seeing of 1.″4–1.″6 so that the Strehl ratio after closing the AO loop was about 25.5%. The secondary component was already visible on the noncoronagraphic image, as seen in Figure 10. The angular separation measured on the coronagraphic image ($\rho = 0.''169$) does not match the separation in the noncoronagraphic image ($\rho = 0.''092$), which is closer to the *Hipparcos* value ($\rho = 0.''097$). Actually, since the companion is clearly visible on the coronagraphic image, it strongly affects our centering ability, and that probably explains this discrepancy. The jitter was also quite large, and the companion intensity fluctuated a lot on individual exposures so that on average its brightness was fainter. The corrected photometry gives a star-to-companion brightness ratio of 2.3 (0.92 mag), in agreement with the measurement for the unocculted image.

4.2. Circumstellar Disks

In the past few years, several circumstellar disks around relatively young stars have been discovered, thanks to the capabilities of Lyot coronagraphs both in space and on the ground (Smith & Terrile 1984; Jayawardhana et al. 1998; Augereau et al. 1999). We revisited some of these objects on 2004 April 7 and 8 to probe the very close environment of these young massive stars (HD 100546, HD 141569, and HR 4796). No additional structures were observed at close radii, putting some new constraints on the dust distribution. Some well-known features were marginally detected. Other Herbig AeBe stars featuring far-IR excess were observed, but no circumstellar emissions were detected (HD 149914, HD 169142 and HD 100543). Below, we present the results for the star HD 100546.

HD 100546 ($V = 6.7$, $K = 5.4$) was observed on 2004 April 7 with the IB2.18 filter. The total integration time was 480 s for the object and the calibrator star to be subtracted out. To preserve the pupil orientation, the calibrator was selected at the same declination, with a R.A. difference of 1 hr (assuming 1 hr of telescope time per target), so that the parallactic angle was comparable to the one for the target star. The disk, which was previously observed by Augereau et al. (2001) with the *Hubble Space Telescope* (*HST*), was detected with the FQPM as an extended emission with no particular structures from about 0.″5 out to 1.″62 (Fig. 11). Using the outer edge of the detected disk, we measured an orientation of P.A. = 165° ± 5° and axis ratio of 0.84 ± 0.02 (measured by ellipse fitting to contour lines at 1.″4), consistent with *HST* data. At closer separations (<0.″5), the residual was very likely a result of the subtraction process between the star and the calibrator, which is not optimal. Static aberrations were indeed stronger for the object, although the Strehl ratio was of about 30% for both the object and the calibrator. This area was numerically cancelled in Figure 11.

The surface brightness (corrected from the color index *H–K*) differs from the one measured by Augereau et al. (2001) by almost 1 mag arcsec^{-2} because its measurement is corrupted by the large amount of diffraction residual at close separations. In addition, the determination of the intensity scaling factor (between the star and the calibrator) becomes difficult because the disk is visible at any P.A. (position angle with respect to the north) and any separation (usually this factor is estimated in a region dominated by diffraction residual alone). The plots in Figure 12 show the radial profiles of the disk along the major and minor axes (at respectively P.A. = 165° and 75°), and Figure 13 gives the limit of detection for a pointlike object. For comparison, we also give the same plots for the star HD 149914 (similar observing conditions), for which no circumstellar emission was detected to estimate the residuals. In such

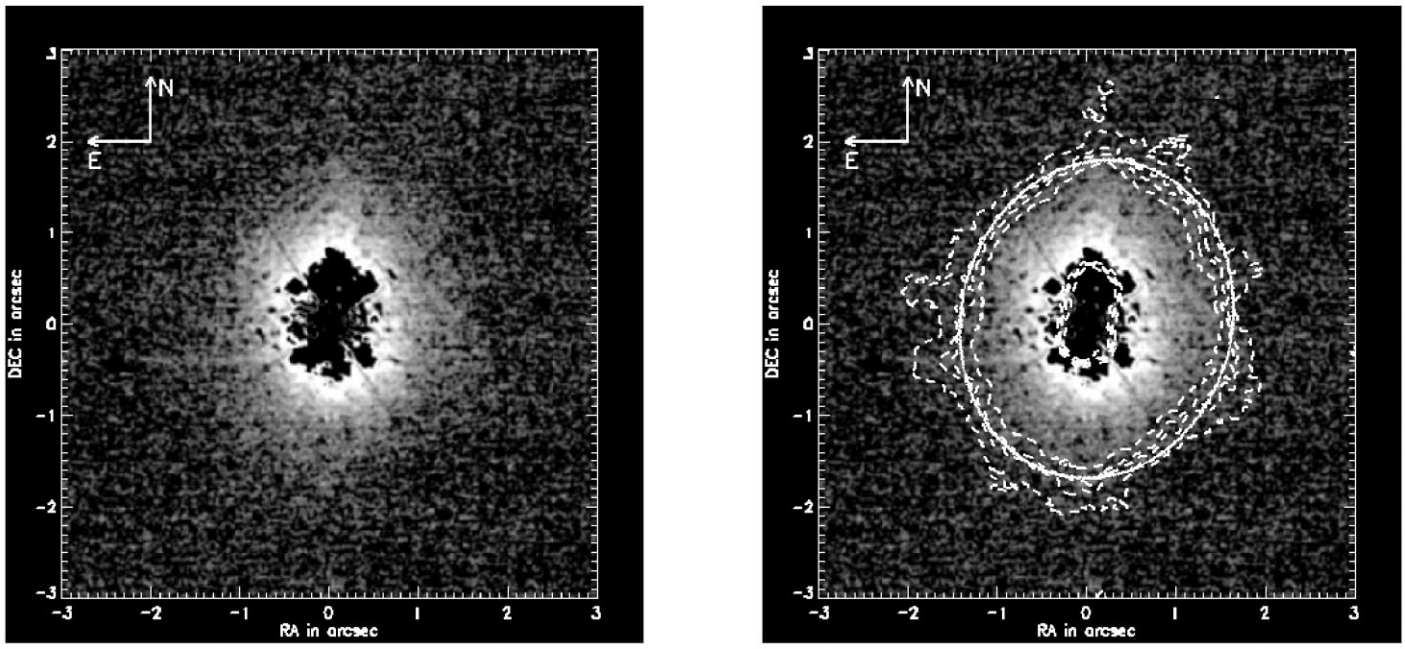

FIG. 11.—Coronagraphic image of HD 100546 subtracted with a calibrator star (*left*). The same image is also displayed using contour lines overlaid with the fitted ellipse (*right*). The central part was numerically cancelled, since we believe that no information can be retrieved in this region. The orientation (P.A. = 165°) and axis ratio (0.84) of the disk are in agreement with previous observations. The field of view is 6″.

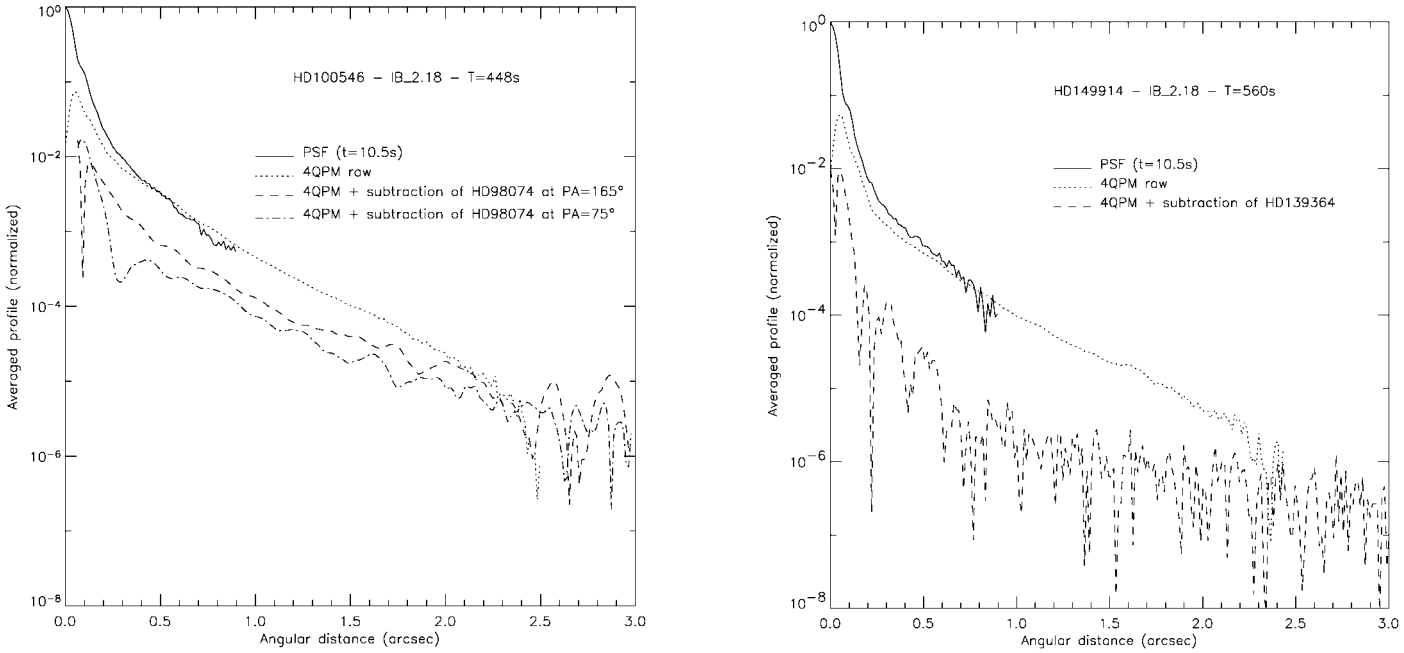

FIG. 12.—Radial profiles of the disk around HD 100546 at P.A. = 165° and 75° (*left*). The comparison with the radial profile of HD 149914 (*right*) emphasizes the presence of the extended emission beyond 0.″5 (much larger attenuation is achieved in this case with the reference star subtraction).

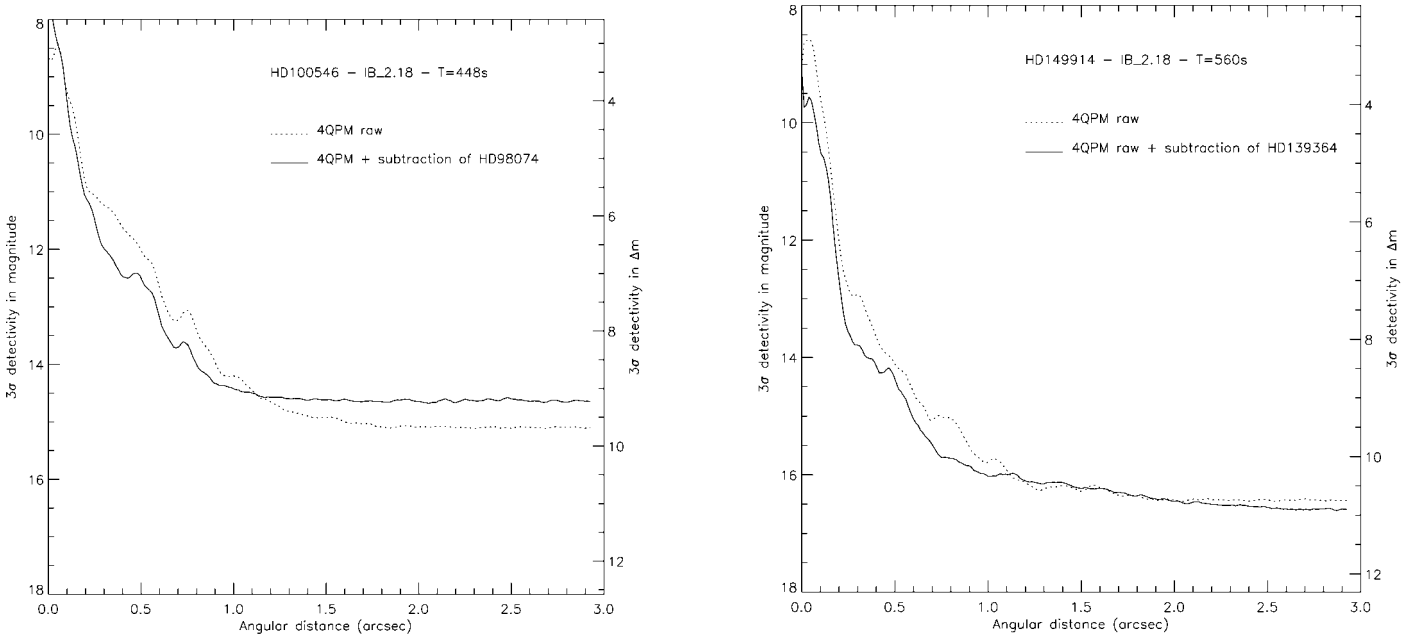

FIG. 13.—Limit of detection for a pointlike object at 3 σ for HD 100546 (*left*) and HD 149914 (*right*). At 0.″5, the FQPM allows detection of a companion 9 mag fainter than the star. The subtraction of a calibrator improves the detectivity at close separation, but increases the noise in the background-limited region (typically beyond ~1.″2).

conditions, the limit of detection at 0.″5 corresponds to a pointlike object 9 mag fainter than the star. We measured better detectivity at large radii for the image of HD 149914. This improvement of 0.83 mag results from two differences: (1) an apodized stop was used for HD 100546, while HD 149914 was observed with a full undersized stop (the difference of transmission amounts to 0.36 mag), and (2) the number of frames is larger by a factor 2.5 for HD 149914, thus generating a lower background noise by 0.49 mag (the background is essentially readout noise limited in the narrowband filter IB2.18).

We also found a faint structure on the calibrator star image, possibly a companion 6.25 mag fainter and located at 0.″48 (Fig. 14).

In the background-limited region, the detection threshold at 3 σ is about 15.3 mag, while the exposure time calculator (ETC) for NACO predicts 17.05 mag. The same difference was noticed for all our sample stars. After careful inspection of the background and detector noise, we concluded that the stellar flux was overestimated by 1 mag by the ETC, which partially accounts for the difference in limiting magnitude. Another, additional source of noise might be responsible for the loss of performance. In 2004 May, the NACO detector was replaced with a new array that provided a larger full well (a gain of a factor of 5), which we expect to be more appropriate for imaging circumstellar disks.

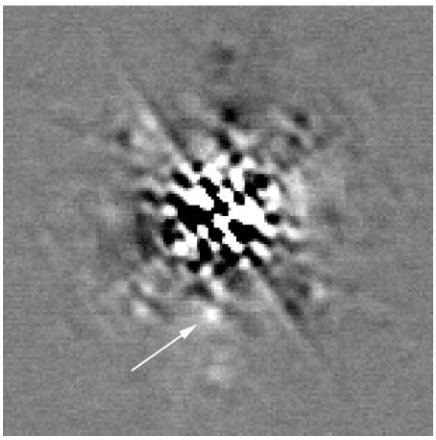

FIG. 14.—Coronagraphic image with a 2″ field of view (as on Fig. 11) with an additional centrosymmetrical subtraction to remove the disk component. A pointlike object possibly associated to the calibrator star is detected at 0.″48 with a magnitude difference of 6.25 (positive intensities correspond to the calibrator star contribution).

4.3. Extragalactic Sources

Nearby active galactic nuclei (AGNs) are another source of interest for the application of the FQPM. The challenge is quite similar to that of stellar environment, since the bright core—with an underlying central engine—is usually unresolved and can therefore be attenuated with a coronagraph. Nevertheless, such objects can be relatively faint, and we cannot expect a large Strehl ratio. As a result, the effect of the coronagraph is mostly a gain in sensitivity at large angular radii. Because the FQPM avoids saturation and allows deeper integration, a better signal-

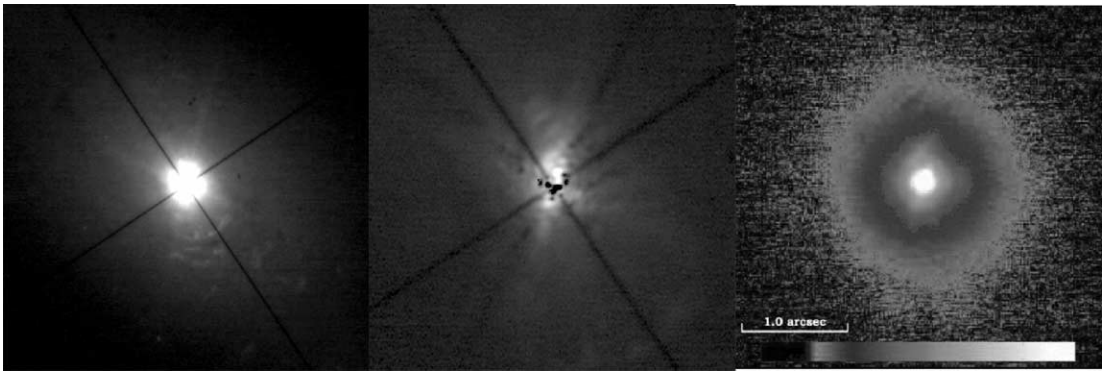

FIG. 15.—Images of the AGN NGC 1068 with the K_s filter. *Left*: large-field (11.″7) FQPM image (2003 November); *middle*: FQPM image subtracted with a reference star (FOV = 3.″5); *right*: a direct image in K_s band from Gratadour et al. (2004; no coronagraph, FOV = 3.″5). Not a linear intensity scale. North is up, east is left.

to-noise ratio is achieved in a background- and/or detector-limited area. The case of NGC 1068 is unique, since it is a bright object ($B = 9.03$, $K = 7.27$) for which we can expect a significant gain at close separation. This well-known AGN was observed in 2003 November by one of us (D. G.) in the K_s filter and also during the commissioning run, although with a much lower Strehl ratio (1.″2, Strehl ≈30%). The data obtained on 2003 November more clearly demonstrate the current interest in using a coronagraph on these types of objects, because the seeing was definitely more favorable (<0.″7, Strehl ≈60%). The FQPM delivers unprecedented snapshots of the environment around NGC 1068. The images are displayed in Figure 15. Many complex structures are revealed by the coronagraph. Some of them were identified previously by Rouan et al. (2004), although in the *L* and *M* bands. First of all, the coronagraphic attenuation of the central object allows deeper integrations, revealing large-scale, arclike structures to the southwest, extending from 1.″7 to 5.″6 from the core and aligned with the ionization cone axis. These were not detected in the *L* and *M* band images. We also detect the same patterns identified by Rouan et al. (2004), including the microspiral to the north, bending clockwise with a length of about 20 pc. A corresponding symmetrical but fainter structure is visible to the south of the nucleus, called the "south tail" in Rouan et al. (2004). North of the microspiral, a series of four elongated knots is aligned at P.A. = 25°. These structures can be explained by the interaction of a radio jet with the interstellar medium. A new unresolved spot is also revealed between the first and second knots. Finally, an unidentified structure is clearly visible to the west of the nucleus. A more detailed study of these data will be given in Gratadour et al. (2004).

5. COMPARISON WITH OTHER DESIGNS

Many high-contrast techniques have been proposed in the last few years, but only a few of them have been tested on the sky. These include the Achromatic Interfero Coronagraph (AIC; Gay & Rabbia 1996), the shaped pupil mask (Debes et al. 2002), the simultaneous differential imager (SDI; Close et al. 2004), and the nulling interferometer (Liu et al. 2004). The FQPM can be compared with these new devices, but it is important to keep in mind that a coronagraph (or any light-suppression device) is only reducing the contribution of the coherent light. Given that, the on-axis light rejection mostly depends on AO performance, rather than the coronagraph capabilities (which are always good, compared to the residual aberrations provided by current AO systems).

The raw images delivered by the FQPM on NACO provide on average a minimal contrast of 10 (near the center) and 10^3 at 0.″5. Using the AIC on a 1.5 m telescope, Baudoz et al. (2000) obtained a contrast of about 50 at the center and 300 at 0.″5 in the *K* band. The shaped pupil-mask technique was tested at the Mount Wilson 100 inch (2.5 m) telescope, but no significant improvement in contrast was noted for separations smaller than 0.″5. However, observations were carried out in the visible with a low Strehl ratio. At mid-IR wavelengths, Liu et al. (2004) reached a total rejection of 30 using a nulling interferometer on the MMT. The contrast definition is not applicable with interferometers, but such performance is very good (see Table 1 for comparison with theoretical rejection) and is the result of a large Strehl ratio (probably more than 90%). SDI is a new observing mode of NACO that provides simultaneous imaging of two narrow bands located in and out of the methane absorption feature in the *H* band. The stellar spectra are flat in this region, while planetary companions show a noticeable contrast between the two bands. Therefore, the speckle noise can be efficiently reduced when the two images are subtracted out after homothetic rescaling. Close et al. (2004) claim to reach a contrast of 10^5 at 0.″5, while the FQPM provides a contrast of about 3×10^4 when a calibrator is subtracted. The simultaneous calibration is obviously more efficient for that purpose. However, the use of the SDI is restricted to the search for methane companions only.

This simple comparison shows that the FQPM, when installed on NACO, delivers a contrast that is better or comparable to other light-suppression designs (for similar Strehl ra-

tios), and this performance is mainly set by the residual phase aberrations.

6. CONCLUSION

The FQPM was installed inside NACO and was successfully commissioned, although seeing conditions were variable (0.″6 to 2.″6, with coherence times as small as 3 ms). Despite poor AO compensation, the observed performance is in agreement with theoretical expectations. The chromatism effect is totally negligible for spectral resolution larger than about 6, which is always the case for the NACO imaging modes. The attenuation factor is limited by the image motion (residual jitter) and low-order phase aberrations. A comparison with the Lyot coronagraph shows that the FQPM is complementary to the Lyot and can reach a larger contrast at close angular separations ($\rho <$ 0.″35). The Lyot allows deeper integration at large radii and reduces the readout noise, since the central peak attenuation is much larger than for the FQPM.

A dedicated observing strategy is required to take advantage of the FQPM capabilities. Centering must be performed accurately using a flat-field image to define the mask location. This position is expected to evolve with the instrumental flexures and should be monitored throughout the night and sometimes several times for each object (if very close to zenith). The static defocus introduced by the FQPM thickness also needs to be compensated for, but this is now performed automatically once the FQPM is selected. In addition, NACO includes a derotator to prevent field-of-view rotation (caused by the alt-azimuthal telescope mount). As a result, the pupil image at the cold stop position rotates, and a careful alignment is required with the apodized Lyot stop to mask the secondary mirror support. The apodized stop therefore reduces the diffraction spikes. However, the fast rotation of the pupil image at high elevations makes this stop useful only for objects at large air masses (>1.4). For smaller air masses, we recommend to use the undersized stop. In that case, however, the choice of a calibrator star (to subtract the residual static speckles) is very critical and must be searched for at the same parallactic angle as the target so that the spikes have the same orientation on both objects. Finally, calibration of radial attenuation might be needed to recover the photometry of off-axis objects at small angular radii (close binaries, for instance).

The scientific capabilities of the FQPM were also demonstrated by the observation of NGC 1068, for which an unprecedented contrast was reached at small separations. As for the circumstellar disks, no additional features other than those already known were discovered. Some large-scale features were marginally detected on HD 100546, HD 141569, and HR 4796.

Finally, we point out that an achromatic version of the FQPM would have the advantage of being used with any near-IR filter of NACO. For instance, a FQPM also operating in the *H* band could be combined with the recently installed simultaneous differential imager (Close et al. 2004) to improve the search for methane companions like giant extrasolar planets around nearby young stars. We are indeed conducting a technical development program to develop such an achromatic device.

Coronagraphs and other light-suppression devices are now able to provide a very large rejection of on-axis objects, as demonstrated by laboratory experiments (Riaud et al. 2003, for instance), but their capabilities on the sky are damped by the large amount of residual phase aberrations that are left uncorrected on ground-based instruments. Significant efforts must now be made on AO systems in order to approach the detection limit for extrasolar planets.

We would like to thank the ESO staff at Garching and Paranal for making the implementation of the FQPM inside NACO possible. We are sincerely grateful to N. Ageorges (ESO) for supporting the day and night commissioning in 2004 January.

REFERENCES

Augereau, J. C., Lagrange, A. M., Mouillet, D., & Ménard, F. 1999, A&A, 350, 51
———. 2001, A&A, 365, 78
Baudoz, P., et al. 2000, A&AS, 145, 341
Boccaletti, A., Riaud, P., & Rouan, D. 2002, PASP, 114, 132
Boccaletti, A., Riaud, P., Rouan, D., & Baudrand, J. 2003, Proc. SPIE, 4850, 556
Close, L., Lenzen, R., Biller, B., Brandner, W., & Hartung, M. 2004, in Proc. ESO Workshop, Science with AO, ed. W. Brandner & M. Kasper (Berlin: Springer), in press
Debes, J. H., Ge, J., & Chakraborty, A. 2002, ApJ, 572, 165
Gay, J., & Rabbia, Y. 1996, CR Acad. Sci. Paris, 332, 265
Gratadour, D., Rouan, D., Boccaletti, A., Riaud, P., & Clénet, Y. 2004, A&A, in press
Jayawardhana, R., Fisher, S., Hartmann, L., Telesco, C., Pina, R., & Fazio, G. 1998, ApJ, 503, 79
Kuchner, M. J., & Traub, W. A. 2002, AJ, 570, 900
Liu, W. M., et al. 2004, ApJ, 610, 125
Lyot, B. 1939, MNRAS, 99, 580
Matsuoka, J., Kitamura, N., Fujinaga, S., Kitaoka, T., & Yamashita, H. 1991, J. Non-Crystalline Solids, 135, 86
Mouillet, D., Fusco, T., Lagrange, A. M., & Beuzit, J. L. 2003, EAS Pub. Ser., 8, 193
Nisenson, P., & Papaliolios, C. 2001, ApJ, 548, L201
Perryman, M. A. C., et al. 1997, A&A, 323, 49
Riaud, P., Boccaletti, A., Baudrand, J., & Rouan, D. 2003, PASP, 115, 712
Riaud, P., Boccaletti, A., Rouan, D., Lemarquis, F., & Labeyrie, A. 2001, PASP, 113, 1145
Roddier, F., & Roddier, C. 1997, PASP, 109, 815
Rouan, D., Riaud, P., Boccaletti, A., Clénet, Y., & Labeyrie, A. 2000, PASP, 112, 1479
Rouan, D., et al. 2004, A&A, 417, L1
Rousset, G., et al. 2003, Proc. SPIE, 4839, 140
Smith, B. A., & Terrile, R. J. 1984, Science, 226, 1421